Earth Planet. Sci. Lett. 668 (2025) 119567

Contents lists available at ScienceDirect

Earth and Planetary Science Letters

journal homepage: www.elsevier.com/locate/epsl

Crustal structures of giant impact basins on Mars: Implications for crustal accommodation of Hellas, Utopia, Isidis and Argyre basins

Songbai Xuan [a,b], Shuanggen Jin [c,*]

[a] Shanghai Astronomical Observatory, Chinese Academy of Sciences, Shanghai 200030, China
[b] Wuhan Gravitation and Solid Earth Tides National Observation and Research Station, Wuhan 430071, China
[c] School of Surveying and Land Information Engineering, Henan Polytechnic University, Jiaozuo 454003, China

ARTICLE INFO

Editor by: Dr C Carolina Lithgow-Bertelloni

Keywords:
Gravity
Topography
Giant impact basins
Crustal thickness
Crustal accommodation

ABSTRACT

The Hellas, Utopia, Isidis and Argyre (HUIA) basins on Mars are widely regarded as the giant-impact generated quasi-circular depressions. While several models of the crustal and lithospheric structures have been constructed, there remains a worthy question with respect to the mechanism of post-impact crust modification. In this paper, the observed and theoretical admittances for the northern lowlands and southern highlands on Mars are presented. After the effects of Tharsis Rise are removed, the estimated elastic lithosphere thickness suggests a weak lithosphere on Mars. Subsequently, an elastic lithosphere thickness of 10 km is applied to determine the crustal structures and lithospheric stresses using geoid and topography based on the thin shell model. The results show significant relief in the Moho and extensional lithosphere in the HUIA basins. The post-impact crustal accommodation of these basins includes isostatic adjustment, viscous relaxation of the lower crust and basalt infilling, where the Moho relief is mainly controlled by the post-impact isostatic adjustment. In details, Hellas is a fully Airy compensated basin, Argyre exists a possibly relaxed crust, and Utopia and Isidis are infilled by denser volcanic materials.

1. Introduction

The Hellas, Utopia, Isidis, and Argyre (HUIA) basins on Mars are acceptedly produced by the giant impacts. These basins are well-preserved from their formation during the Noachian period (Frey, 2008; Werner, 2008), followed by long-term sediment or basalt loading in the Hesperian or Amazonian era (Jin and Zhang, 2014; Tanaka et al., 2014; Werner, 2009). While these basins have similar ages (Frey, 2008; Werner, 2008), they exhibit obvious differences in the geophysical signatures, especially in gravity anomaly and crustal structure (Neumann et al., 2004; Tenzer et al., 2015; Wieczorek et al., 2022; Zuber et al., 2000), suggesting diverse post-impact evolutionary patterns. In terms of similarity, the Hellas and Argyre basins in the southern highlands present subtle gravity anomalies, and the Utopia and Isidis basins in the northern lowlands exhibit positive gravity anomaly (Konopliv et al., 2016). Crustal structures provide important information for understanding the lithospheric properties and post-impact crustal accommodation of the HUIA basins in early Martian history (Andrews-Hanna et al., 2008; Bottke and Norman, 2017; Mohit and Phillips, 2007; Searls et al., 2006; Solomon et al., 2005).

Although several models constrained by gravity and topography exhibit the crustal structures of the HUIA basins, the mechanisms of the post-impact crustal evolutions remain controversial. The classically inverted crust-mantle boundary (Moho) models show the thinned crust beneath the HUIA basins, especially the Isidis' crust with minimum thickness of ~3 km (Zuber et al., 2000) or ~6 km (Neumann et al., 2004; Wieczorek et al., 2022). In these models, Hellas is expected as an isostatically compensated basin, agreeing with the argument from the thin-shell model with low elastic lithosphere thickness (Searls et al., 2006). However, the larger elastic lithosphere thickness determined by the localized admittance analysis (Deng et al., 2023) suggests a relatively thicker crust for Hellas. Alternatively, Hellas is considered as a buried mascon basin regarding the anomaly to the northeast of the basin (McGovern et al., 2002), which may be the effect of a mantle plume (Broquet and Andrews-Hanna, 2023). For the filled Utopia, the filling materials could be sedimentary (Ding et al., 2019) or denser basalt (Deng et al., 2023; Searls et al., 2006), as either can satisfy all the geological and geophysical constraints. Isidis is acceptedly filled by volcanic materials, but the relative weak (Mancinelli et al., 2015; Zhong et al., 2022) or strong (Ding et al., 2019; Ritzer and Hauck, 2009)

* Corresponding author.
E-mail addresses: sgjin@shao.ac.cn, sgjin@hpu.edu.cn (S. Jin).

https://doi.org/10.1016/j.epsl.2025.119567
Received 27 April 2025; Received in revised form 4 July 2025; Accepted 1 August 2025

lithosphere would support different volume of volcanic components. For Argyre, sedimentary infilling (Ding et al., 2019) and viscous relaxation of the lower crust (Mohit and Phillips, 2007) are proposed to explain the modified crust.

In this study, the elastic lithosphere thickness is estimated by comparing the observed admittances with theoretical admittances assuming the Airy, Pratt and flexural isostasy. Subsequently, the crustal thickness, density variations and lithospheric stresses of the HUIA basins are determined based on the thin-shell model proposed by Banerdt (1986) and updated by Broquet and Andrews-Hanna (2022). Finally, the mechanism of post-impact crustal accommodation for the HUIA basins are discussed.

2. Datasets and spectral analysis

2.1. Topography and gravity data

The spherical harmonic coefficients used in this study are from the topography model MarsTopo2600 (Wieczorek, 2015) and the gravity model JGMRO120D (Konopliv et al., 2016). These models are originally extended up to spherical harmonic degree/order 2600 and 120, respectively. MarsTopo2600 is truncated up to degree 120 to be consistent with the degree/order 120 of the gravity model JGMRO120D. In consideration of the center-of-mass coordinate system and the rotational contribution of the planet, the spherical harmonics of degree 0 and the zonal harmonic of degree 2 of topography and gravity are not included in this study. The Gaussian filter of 100 km radius is applied to attenuate the short-wavelength components of topography and gravity data. Another role of the filter is to remove the stripe noises on the map of the gravity anomaly, especially in the northern hemisphere (Supplementary Fig. S1). After above processing, we obtain the new spherical harmonic models of the topography and gravity, and the corresponding topography, gravity anomaly and geoid are shown in Figs. 1a-c. For the long- and medium-wavelength features, these maps do not differ significantly from the previous published models at the global scale.

2.2. Spectral analysis

The power spectra of the topography, gravity anomaly and geoid from the above models are plotted in Fig. 1d. The decays of the topographic and geoid powers are similar to the initial models (Wieczorek, 2015) at the degrees less than 30. However, due to using a Gaussian

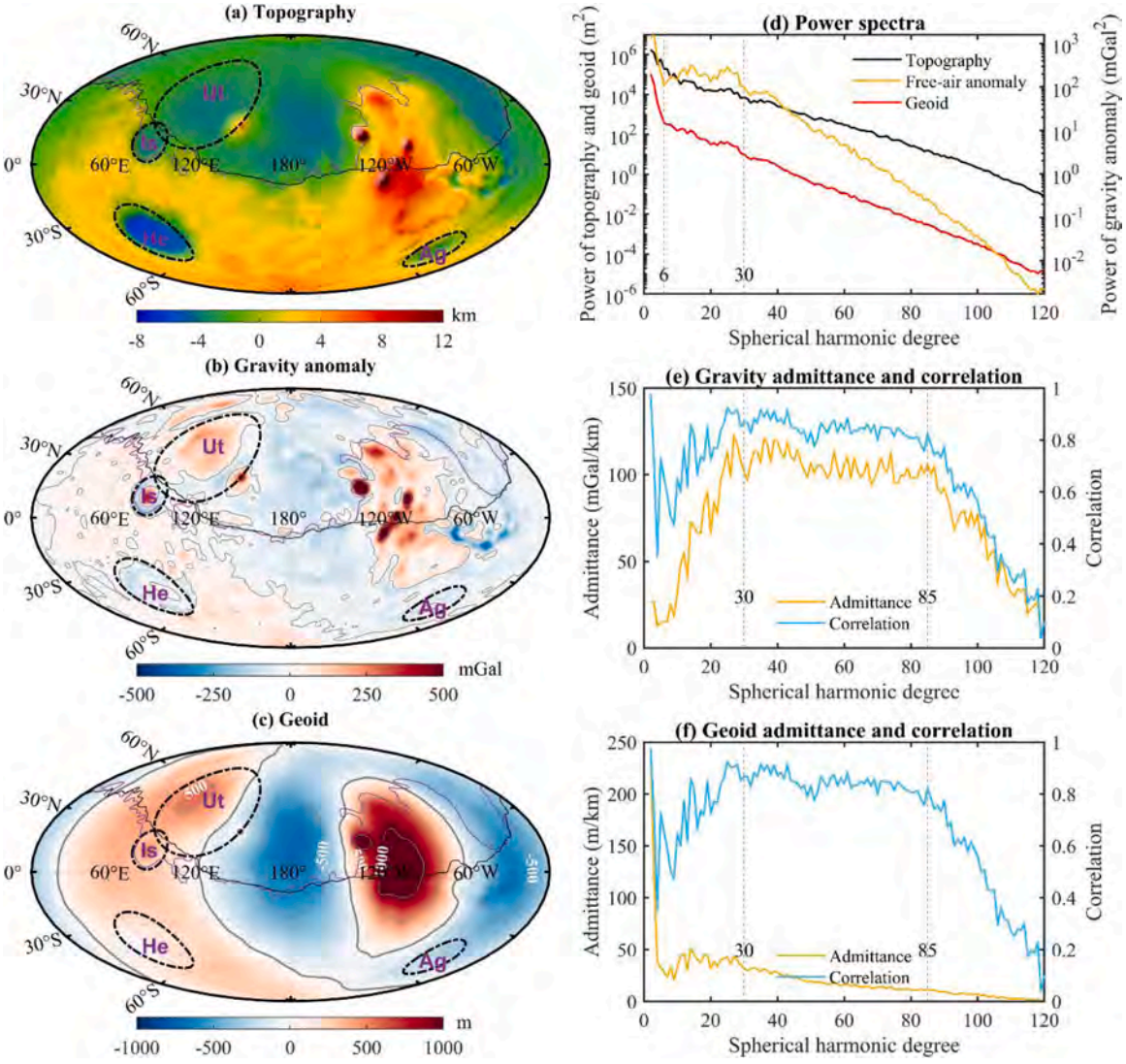

Fig. 1. (a) Topography, (b) gravity anomaly and (c) geoid of Mars presented in the Hammer-Aitoff projection with the central meridian of 180°E. Purple curves indicate the putative Martian paleoshorelines of the Arabia ocean (Parker et al., 1993). Black curves indicate the dichotomy boundary from Andrews-Hanna et al. (2008). Black dashed circles are four giant-impact basins proposed by Frey (2008): He, Hellas; Ut, Utopia; Ag, Argyre; Is, Isidis. (d) Power spectra of topography, free-air anomaly and geoid. (e) Free-air anomaly admittance and correlation. (f) Geoid admittance and correlation.

filter, the lower amplitudes and the higher slopes occur for the power spectra beyond degree 50. Referring to the power spectra from the observed models (Supplementary Fig. S2), the nonlinear decays beyond degree 50 on log-log plot are not in accordance with the power law manner on Venus (Pauer et al., 2006). In comparison with the power spectrum of topography, the geoid has a significantly higher slope at the degrees 2-6, resulting from the lithospheric loads and deflection of the Tharsis province (Phillips et al., 2001; Wieczorek, 2015). Additionally, the larger value of the power spectrum of the gravity anomaly at the first 5 degrees (2-6) can also be attributed to the mass of Tharsis Rise (Phillips et al., 2001; Zuber and Smith, 1997). Comparing the topography and geoid, a constant value at the degrees 6-30 is the most prominent characteristic, suggesting the long-wavelength surface topography would be isostatically compensated in the lithosphere (Turcotte et al., 2002).

The admittance and correlation spectra between the topography and gravity anomaly shown in Fig. 1e are consistent with the results from the initial models (Wieczorek, 2015). The admittance spectrum has an increasing trend at the relatively lower degrees (less than 30) and a decreasing trend at higher degrees (beyond 85). At medium degrees (30-85), the admittance maintains at a larger amplitude of ~100 mGal/km, which would be expected for compensation of the surface topography (see next section for details). In contrast, the admittance between the topography and geoid presents lower values with the exceptions of degrees 2 and 3 (Fig. 1f). This larger admittance at degrees 2 and 3 suggests the dynamic contributions dominate the long-wavelength geoid signal (Zhong and Roberts, 2003). The correlations between topography and gravity/geoid the high values between 0.8 and 0.9 at the medium degrees (Fig. 1e-f), which supports a nearly constant density of the Martian crust.

3. Isostatic compensation of Mars

The mass deficit or excess from the surface topography of a terrestrial planet can be compensated by several mechanisms, such as crustal thickness variations (Airy compensation), density variations in the crust and mantle (Pratt compensation) and lithospheric deflection (flexural compensation). For Mars, the hemispheric dichotomy and Tharsis Rise are two prominent features on the surface of the planet. Under consideration of these features, the admittances between the topography (Fig. 1a) and gravity anomaly (Fig.1b) are applied to investigate the modes of compensation of the lowlands and highlands.

3.1. Division of the southern highlands and northern lowlands

The hemispheric dichotomy on the surface topography of Mars is an ancient feature (Solomon et al., 2005). Topographically, the putative Martian paleoshorelines of the Arabia Ocean (Parker et al., 1993; Sholes et al., 2021) is pronounced in distinguishing the northern lowlands from the southern highlands (Fig. 1a). In this way, Tharsis Rise is included in the southern highlands and the Isidis basin belongs to the northern lowlands. Alternatively, the boundaries of the hemispheric dichotomy is presumably buried beneath Tharsis Rise in the western hemisphere according to the crustal thickness (Zuber et al., 2000). Andrews-Hanna et al. (2008) proposed a dichotomy boundary explained by a giant impact. This boundary can be accurately fitted by an ellipse. Here we would separate the topography and gravity anomaly to northern and southern parts in space domain along the two typical boundaries of Sholes et al. (2021) and Andrews-Hanna et al. (2008). Subsequently, the separated topography and gravity anomaly would be completely expanded to the spherical harmonic coefficients up to degree/order 120 for calculating the gravity admittances.

3.2. Localization of topography and gravity of Tharsis Rise

Tharsis Rise likely originated from one or more long-lived mantle plumes after the formation of the crustal hemispheric dichotomy (Solomon et al., 2005). To characterize the topography and gravity anomaly of Tharsis Rise, we used the technology of the localization on the sphere with the band-limited Slepian functions (Simons et al., 2006; Wieczorek and Simons, 2005). We selected the spherical cap with the center location (115°W, 0°N) and angular extension of 60 degrees as the localization region. Slepian_alpha software (Harig et al., 2015) archived at https://github.com/csdms-contrib/slepian_alpha is employed to calculate the Slepian basis functions and eigenvalues. In the study area, the topography and gravity anomaly in spatial domain on 5000 random points are extracted as the observation data. The threshold value of 0.01 (λ_0) for an energy concentration ratio (λ) is selected to determine the number of the used Slepian basis functions (J). The spherical harmonic coefficients of the localized topography and gravity anomaly are determined using the method of least squares. The results are shown in Fig. 2. With the maximum degree/order of 120 for gravity model JGMRO120D, there are 14641 Slepian basis functions but only 2891 functions yield the concentration ratio greater than 0.01 (Fig. 2a). The localized topography (Fig. 2b) and gravity anomaly (Fig. 2c) are concentrated in the Tharsis region compared to the observed images shown in Figs. 1a and 1b, which suggests the localized spherical harmonic coefficients could completely characterize the topography and gravity anomaly of Tharsis Rise.

3.3. Gravity admittances and isostatic analysis

The degree-dependent admittances of the northern lowlands and southern highlands are calculated according on the separation of the topography and gravity anomaly along the boundaries between them including and excluding Tharsis Rise (Figs. 3 and 4). The theoretical gravity admittances assuming Airy, Pratt and flexural compensation are also presented for comparisons with the observed admittances. The zonal harmonic of degree 2 of gravity has been set to 0, which is consistent with the assumption of hydrostatic equilibrium of the planet, indicating that the comparison of the theoretical and observed admittances are comparable. The admittances from Airy and Pratt models including the equal mass and equal pressure are calculated using the formulas of Hemingway and Matsuyama (2017). The admittances from flexural model with parameters listed in Table 1 are calculated following Turcotte et al. (1981).

3.3.1. Tharsis Rise included

The global observed admittance shown in Fig. 1e with standard deviation (1 sigma) is presented in Fig. 3 for comparison with the theoretical admittances. As mentioned above, the observed admittance increases at the degrees 5-30 and nearly maintains a constant at the degrees 30-85. This feature is similar to the theoretical admittance assuming Airy isostasy with compensation depth of 300 km (Figs. 3a and 3d), but the former is about 20 mGal/km less than the latter at the degrees 45-85. The larger admittance of ~100 mGal/km would be expected to the surface topography (Wieczorek, 2015). In the case of the Airy compensation, the theoretical admittance depend on the compensation depth and the mean crustal density (Hemingway and Matsuyama, 2017). When the parameters listed in Table 1 are used, the observed admittance supports the compensation depth of 100-200 km at the degrees 5-85 (Fig. 3a), agreeing with that of Arkani-Hamed (2000). If the mean crustal density of 2900 kg/m^3 is taken the place of a low crustal density of 2582 kg/m^3 (Goossens et al., 2017), the theoretical admittance would decrease and the compensation depth would be ~300 km. For the Pratt compensation (Figs. 3b and 3e), the curves of the theoretical admittance cannot effectively characterize the observed admittance at the low- and intermediate-degrees. The theoretical admittance of the flexural compensation with elastic lithosphere thickness of 100 km has a good fit with the observed admittance at degrees 10-40 (Figs. 3c and 3f), suggesting the topography in this wavelength is supported by the relative strong lithosphere at the global scale. A near

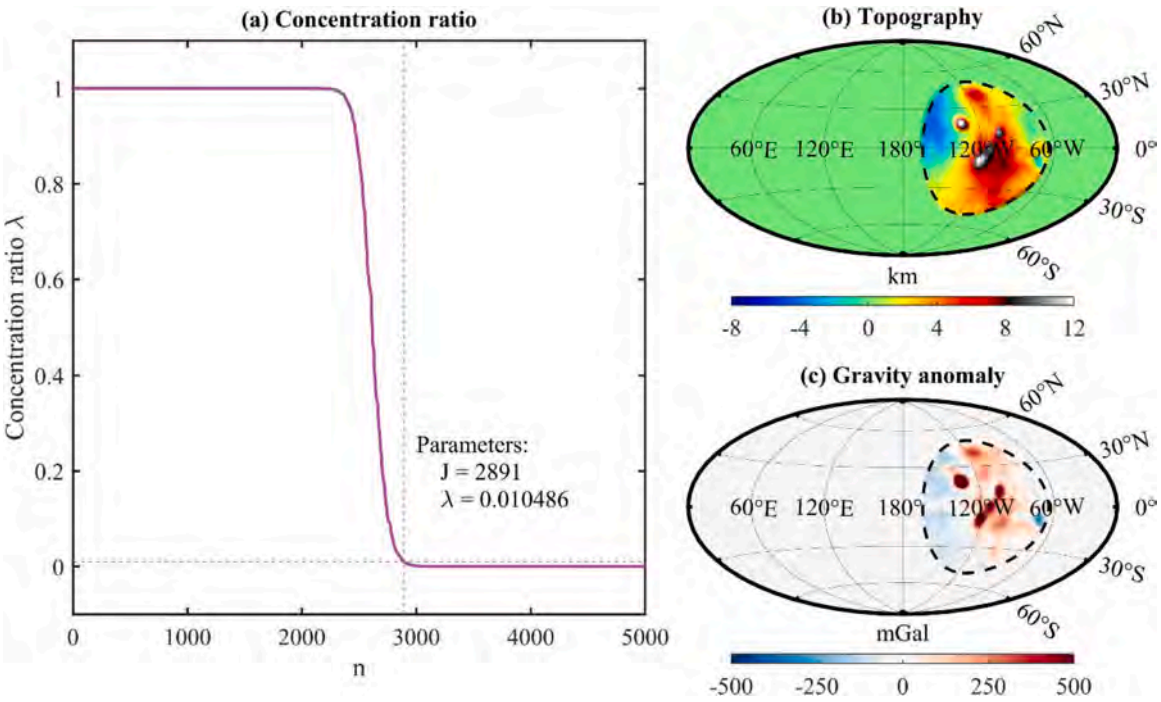

Fig. 2. Localization of Tharsis Rise. (a) Concentration ratio of the Splepian basis functions sorted in a descending order, (b) topography and (c) gravity anomaly. Maps in (b) and (c) are presented in the Hammer-Aitoff projection with a central meridian of 180°E.

constant value of ~120 mGal/km at the degrees 45-85, agreeing with the Airy isostasy (Figs. 3a and 3d), is about 20 mGal/km greater than the observed admittance.

As shown in Fig. 3, the admittances of the northern lowlands and southern highlands present significant differences in characteristics for the both strategies of the observed data division. We firstly concentrated on the topography and gravity anomaly separated the by the putative paleoshorelines of the Arabia Ocean (Figs. 3a-c). For the southern highlands, it is nearly consistent with the global values at the degrees 2-30, linearly decreased with increasing degree at degrees 30-80, and has a relative constant of ~35 mGal/km beyond degree 80. However, it is almost less than 50 mGal/km, attaining a relatively constant of 35 mGal/km beyond degree 25 for the northern lowlands. At low- and intermediate-degrees, the topography of the southern highlands is compensated by lithospheric root (Fig. 1a) or supported by the relative strong lithosphere (Fig. 1c).

Another boundary of hemispheric dichotomy proposed by Andrews-Hanna et al. (2008) is used to separate topography and gravity anomaly of the lowlands and highlands. Figs. 3d-f reveal that the admittance of the northern lowlands is consistent with the values of the global data at degrees 2-30. It rapidly decreased from ~100 mGal/km at degree ~30 to ~50 mGal/km at degree 40 and eventually has a relative stable value of ~30 mGal/km beyond degree 70. We suggest that the surface topography of the northern lowlands should be compensated with the compensation depth of ~200 km assuming Airy isostasy (Fig. 3d) or the supported by the rigid lithosphere with the elastic lithosphere thickness of 100 km (Fig. 3f). For the southern highlands, the characteristics of the admittance revealed the compensation depth should be 50-100 km assuming Airy isostasy (Fig. 3d) or 100-200 km assuming Pratt isostasy (Fig. 3e) at degrees less than 40. It decreased at degrees 30-85, and nearly has a constant of ~30 mGal/km beyond degree 80.

3.3.2. *Tharsis Rise removed*

The topography and gravity anomaly of Tharsis Rise (Fig. 2) are removed from global data (Figs. 1a and 1b). These obtained data are completely extended to the spherical harmonic coefficients with degree/order 120. Non-Tharsis admittances of the global, northern lowlands and southern highlands are presented in Fig. 4.

In comparison with the global admittance including Tharsis Rise (Fig. 3), the observed non-Tharsis admittance increased gradually and fitted the theoretical admittances better at degrees less than 85. For local isostasy, the compensation depth would be at the range of 50-100 km, assuming Airy isostasy (Figs. 4a and 4d) or 100-200 km assuming Pratt isostasy (Figs. 4b and 4e). It is generally consistent with the theoretical admittance of the flexural isostasy with the elastic lithosphere thickness of 10 km (Figs. 4c and 4f). This low value is close to the previous estimations for several units on Mars (McGovern et al., 2002; McKenzie et al., 2002), including the Tyrrhena Patera near the Hellas basin in the southern highlands (Grott and Wieczorek, 2012) and the Utopia basin in the northern lowlands (Ding et al., 2019; Hoogenboom and Srnrekar, 2006). These features indicated a state of near-isostatic compensation and the weak strength of the lithosphere except for Tharsis Rise.

Whether divisional boundary is the putative paleoshorelines of the Arabia ocean or the hemispheric dichotomy boundary of Andrews-Hanna et al. (2008), the non-Tharsis admittances of the northern lowlands and southern highlands present the compatible characteristics at all degrees. All of admittances increased at degrees less than 40 and decreased at degrees beyond 40 (Fig. 4). The low-degree admittances of the lowlands show more disturbances using paleoshoreline-defined highland-lowland boundary (Figs. 4a-c), whereas the consistent admittances between highlands and lowlands are presented using the hemispheric dichotomy boundary (Figs. 4d-f). At the degrees less than 40, the admittances of the lowlands and highlands are approximately fitted with the theoretical admittances of the Airy isostasy with compensation depth of ~50 km (Figs. 4a and 4d), Pratt isostasy with compensation depth of ~100 km (Figs. 4b and 4e) and flexural isostasy with elastic lithosphere thickness of ~10 km (Figs. 4c and 4f), respectively. Therefore, the long-wavelength (~500 km) topography would be locally compensated. We could argue that the northern lowlands and southern highlands exhibit a similar behavior of the lithosphere, which would support that the Martian lithosphere would be a massive stagnant lid (Grott and Breuer, 2008b).

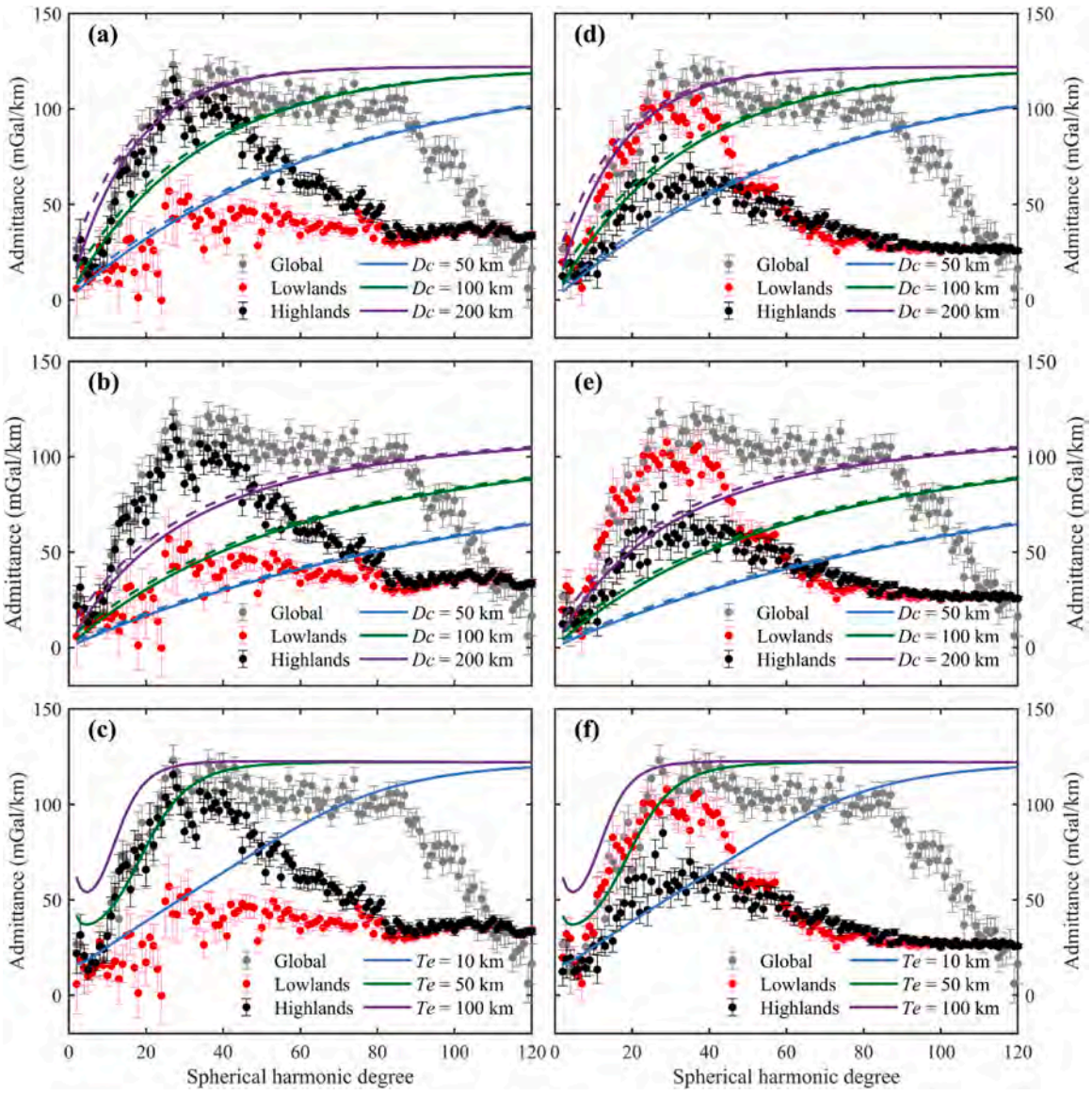

Fig. 3. Comparisons of the observed and theoretical admittances. The northern lowlands and southern highlands are divided by (a-c) the paleoshorelines of the Arabia ocean (Sholes et al., 2021) and (d-f) the boundary of the hemispheric dichotomy proposed by Andrews-Hanna et al (2008).

4. Crustal structures in HUIA basins

4.1. Modeling strategy

To determine the crustal thickness and density anomaly, a thin-shell model developed by Banerdt (1986) with five equations linking eight parameters expressed in spherical harmonics (degree l and order m) is applied here. In this system, the vertical net load (q_{lm}), geoid at Moho (Nc_{lm}), horizontal load potential (Ω_{lm}), lithospheric flexure (w_{lm}), crustal root variations (δc_{lm}) and density variation ($\delta\rho_{lm}$) are constructed into five equations related to the topography (H_{lm}) and geoid at surface (N_{lm}). To model the crustal structures of the HUIA basins, we consider the system updated by Broquet and Andrews-Hanna (2022, 2023), and the details can be found in the Supplementary Material of Broquet and Andrews-Hanna (2023). Given an additional condition, this system yields a unique solution. For the additional condition, Banerdt (1986) set $\delta\rho_{lm} = 0$, $\delta c_{lm} = 0$ and $w_{lm} = kH_{lm}$ corresponding to the assumptions of crustal, mantle and two-level compensation, respectively. Broquet and Andrews-Hanna (2022) set $\delta c_{lm} = 0$ though assuming $w_{lm} = H_{lm}$ and modelling the mantle plume as the internal loading compensated by the dynamic topography. A parameter to measure the ratio of the subsurface load to surface load introduced by Forsyth (1985) would be considered as the additional condition. Belleguic et al. (2005) defined this ratio using the approximation of the mass sheet as:

$$f_{lm} = \frac{\delta\rho_{lm} M}{\rho_i (H_{lm} - w_{lm})} \tag{1}$$

where, ρ_i is the density of the surface load, M is the thickness of the density anomaly located between top and bottom depth. f_{lm} could be assumed a constant equal to f for all degree l and order m. As f is unbounded, the ratio of subsurface loads to total loads varied between -1 and 1 is defined as an alternative parameter (Audet, 2014; Broquet and Wieczorek, 2019; Grott and Wieczorek, 2012). This loading parameter F is given as:

$$F = \frac{\delta\rho_{lm} M}{\rho_i (H_{lm} - w_{lm}) + \delta\rho_{lm} M} \tag{2}$$

where, $F = 0$ corresponds to the surface load only. Given the observed negative topography in giant impact basins, $F < 0$ corresponds to the positive density anomaly. Based on this, we assume the load is located in

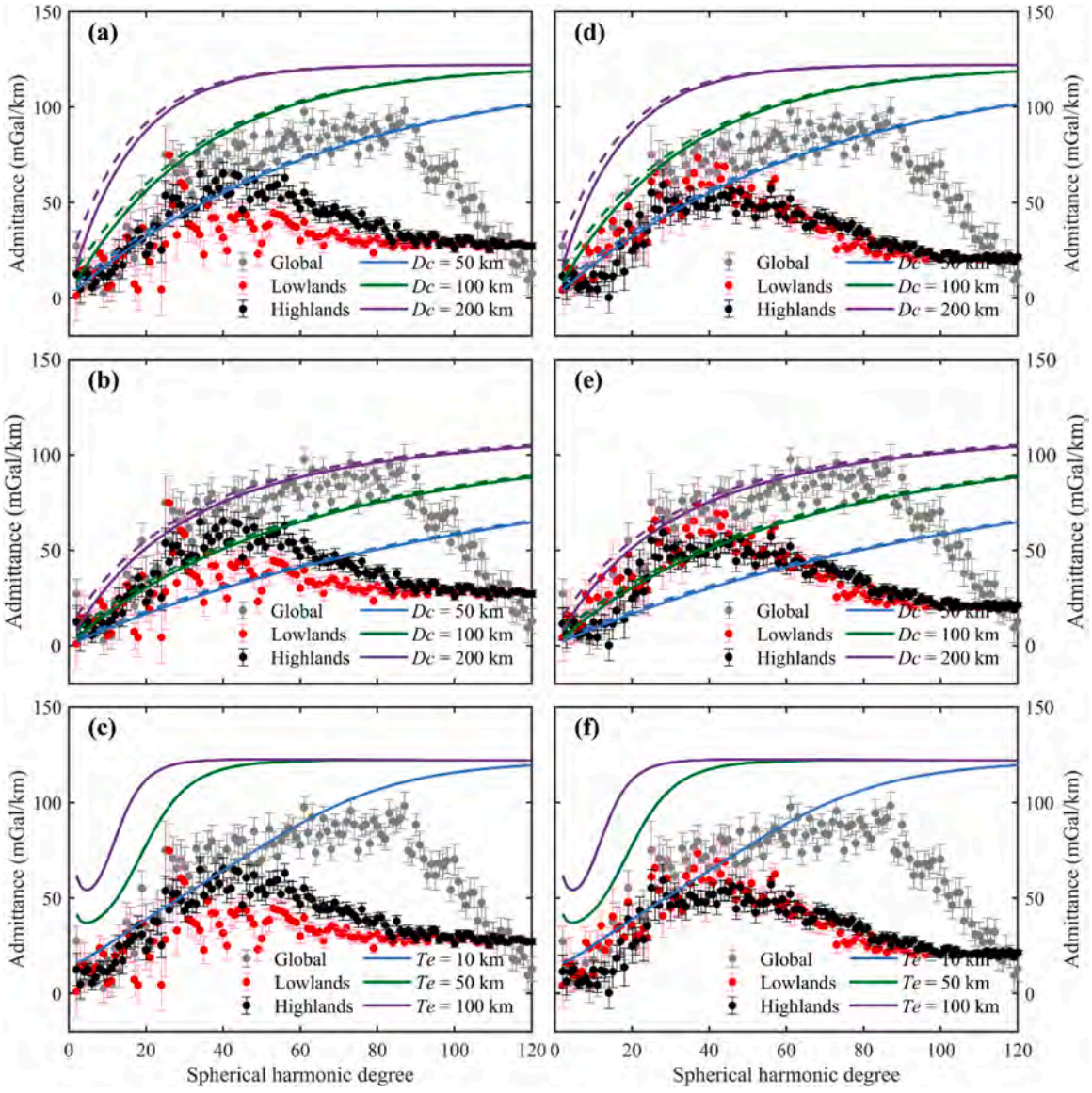

Fig. 4. Same as Fig. 3, but for the non-Tharsis admittances of topography and free-air anomaly.

Table 1
Parameters used for calculations of the admittance.

Parameter	symbol	Value	Unit
Crustal density	ρ_c	2900	kg/m^3
Mantle density	ρ_m	3500	kg/m^3
Mean density of planet	$\overline{\rho}$	3933	kg/m^3
Mean radius of planet	R	3396	km
Reference crustal thickness	T_c	50	km
Young's modulus	E	100	GPa
Poisson's ratio	v	0.25	-
Surface gravitational acceleration	g	3.714	m/s^2
Universal gravitational constant	G	6. 67259×10^{-11}	m^3/(kg·s^2)

the crust with M equal to the reference crustal thickness. In contrast, a negative density anomaly is located in the mantle when $F > 0$.

The relationship between topography H_{lm} and lithospheric flexure w_{lm} given in Eq. (2) is considered as the sixth function, the spherical harmonics of q_{lm}, Nc_{lm}, Ω_{lm}, w_{lm}, δc_{lm} and $\delta\rho_{lm}$ would be exclusively determined when given the loading parameter F, thickness of the density anomaly M and lithospheric elastic thickness. Furthermore, the stresses under purely poloidal component of the tangential displacement can be calculated following Banerdt (1986).

The density of the surface load is set to 2900 kg/m^3 equal to the mean crustal density without loss of generality. The elastic lithosphere thickness for the northern lowlands and southern highlands has been discussed for the cases of including Tharsis and non-Tharsis in section 3. We find that elastic lithosphere thickness of 10 km inferred from the non-Tharsis admittances (Fig. 4) is applicable for the northern lowlands and southern highlands. At these points, the value of the loading parameters F given by Eq.(2) is the only uncertainty, which is crucial in the balance between the crustal thickness and density. According to the negative elevation of the HUIA basins, F could be assumed as the negative values and M is between surface and the depth of 50 km. We used the loading parameters of -0.01, -0.05 and -0.1 to determine the crustal thickness, lateral density variations and lithospheric stresses in the HUIA basins. The lithospheric thickness (not the elastic thickness) of 200 km is applied in this study, which accorrds to assumption of the Martain lithosphere as a stagnant lid. Young's modulus and Poisson's ratio listed in Table 1 are used for computing stresses.

4.2. Crustal thickness and density variation

As the results of crustal thickness and density variations shown in Figs. 5-8, for lower amplitudes of the applied loading parameter, a thinner crust and lower crustal density occurs. Our modeling with three loading parameters (F = -0.01, -0.05, -0.1) yields crustal thickness estimates of 34, 37 and 40 km beneath the InSight landing site (Fig. 6a-c), aligning well with the seismically derived 39 km thickness (Knapmeyer-Endrun et al., 2021). In the case of F = -0.01, the subsurface loads only account for one percent of the total loads, suggesting the contribution of the topography and geoid would mainly be from the variations of the crustal thickness. The minimum crustal thickness is less than 10 km, 15 km and 20 km in the inner areas of the Isidis, Hellas and Utopia basins, respectively (Figs. 5a and 6a). The crustal thickness of the Argyre basin is more than 30 km (Fig. 7a). Negligible anomalies in crustal density are presented beneath these basins (Figs. 5d, 6d and 7d). Comparing to results from F of -0.01, the crustal thickness increases significantly in the Hellas, Utopia and Isidis basins when applying F of -0.05 and -0.1 (Figs. 5a-c and 6 a-c). Accordingly, the significant positive density anomalies are obsvered in these basins (Figs. 5d-f and 6 d-f), especially ~150 kg/m^3 with F of -0.1 (Figs. 5f and 6f). However, the changes in crustal thickness and density anomaly are only ~5 km and ~50 kg/m^3 for Argyre comparing the results from F of -0.01 and 0.1 (Fig. 7).

To directly compare the crustal structures at different F of the HUIA basins, we show the variations in Moho depth on the north-south trending profiles across centers of the craters (Fig. 8). The results from Wieczorek et al. (2022) and Airy isostasy are also presented on the same profiles, where the isostatic Moho are derived from the topography shown in Fig. 1a. The Moho depth with F of -0.01 are nearly in accordance with that of Wieczorek et al. (2022) beneath the inner HUIA basins. The differences in Moho depth out of the HUIA craters between our model and Wieczorek et al. (2022) could be classified into two types. The first is on both sides for the Hellas and Argyre in the southern highlands (Figs. 8a and 8d), and the second is on the south side for the Utopia and Isidis in the northern lowlands (Figs. 8b and 8c). A difference of more than 10 km between the Moho depth with F of -0.01 and 0.1 occurred in the inner Hellas, Utopia and Isidis basins (Figs. 8a-c), but it is less than 7 km for Argyre basin (Fig. 8d). Except for the Hellas basin, the isostatic Moho topography at floor of the other basins shows morphological differences from both our models and those of Wieczorek et al. (2022). Beneath the floor of the Hellas basin, the Moho depth with F = -0.01 is generally consistent with that derived from Airy isostasy (Fig. 8a). Another special case occurs at the Isidis basin, where the isostatic Moho topograpy differs significantly from both our model predictions and those of Wieczorek et al. (2022).

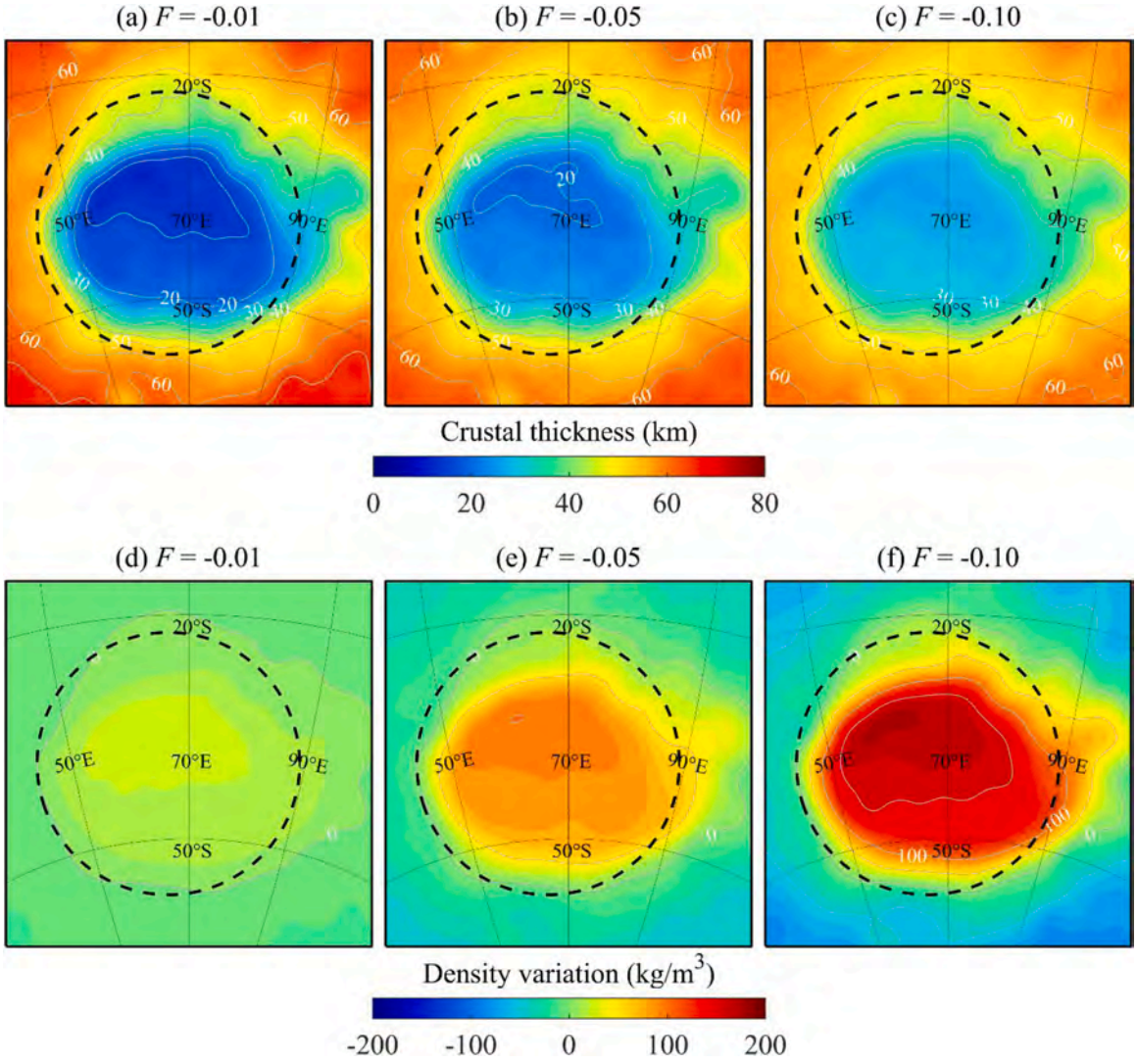

Fig. 5. (a-c) Crustal thickness and (d-f) density anomalies of the Hellas basin with load ratios of -0.01, -0.05 and -0.1. Intervals of the grey contours are 5 km for crustal thickness and 50 kg/m^3 for density variation.

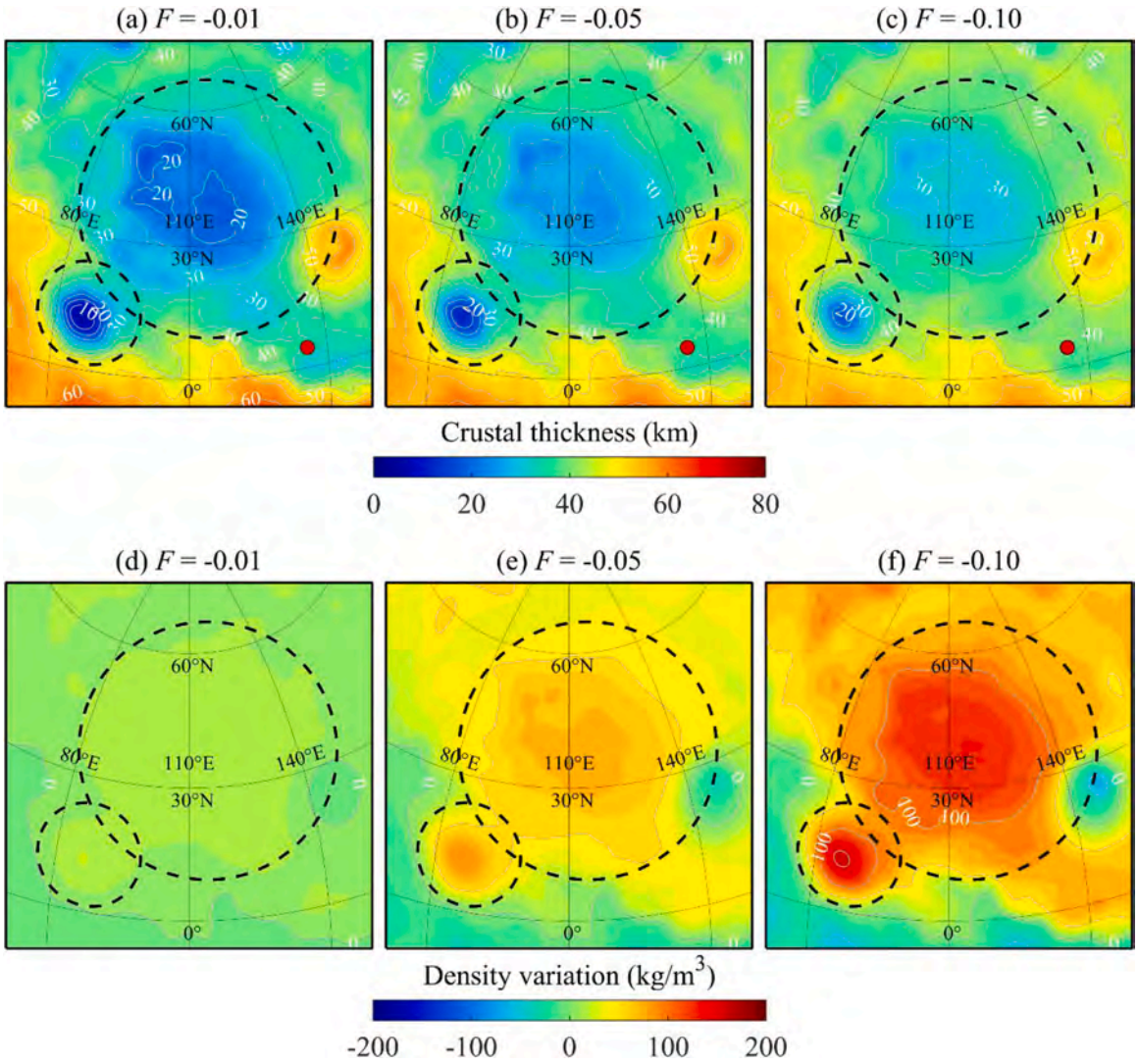

Fig. 6. Same as Fig. 5 but for the Utopia and Isidis basins. The landing site of the InSight mission is marked with red circle in (a-c).

In any case of applied *F*, the crustal root variations are downward in the central Hellas basin (Fig. 8a) and upward in the central Isidis and Argyre basins (Figs. 8c and 8d) compared with the lithospheric flexure. The central Utopia basin exhibits relatively complex crustal root variations (Fig. 8b). These variations show both upward and downward deflections at *F* values of -0.01 and -0.1, while the lithospheric flexure dominates the Moho relief at $F = -0.05$.

4.3. Stresses within lithosphere

The horizontal principlal stresses and their trajectories in the HUIA basins with the lithospheric thickness of 200 km are shown in Fig. 9. Due to the Gaussian filter of 100 km radius applied on the topography and gravity, the maximum principal stresses (σ_1) are almost equal to the minimum principal stresses (σ_3) (Supplementary Fig. S3), i.e. $\sigma_1 \approx \sigma_3$, agreeing with the negligible shear stresses and the hydrostatic lithosphere of Mars (Sleep and Phillips, 1985). It can be seen that the stresses are more closely related to topography (Fig. 1a) than geoid (Fig. 1c). If we use the lower Young's modulus of ~70 GPa and Poisson's ratio of 0.22 (Crane and Rich, 2023), the magnitudes of σ_1 and σ_3 would decrease obviously. Additionally, the amplitudes of σ_1 and σ_3 decrease with decreasing *F*, and the corresponding orientations remain the same. Therefore, the stress characteristics can be represented by the magnitudes and orientations of σ_1, which will be described only in the following contents.

Lateral deformations of the lithosphere are mainly controlled by the extension stresses (positive σ_1) in the HUIA basins, but their distributions present different patterns. For the Hellas basin (Figs. 9a-c), the larger magnitudes of σ_1 occur in the northern region of the basin. Specifically, there exists a region with the maximum σ_1 exceeding 800 MPa in the geographic coordinate window of 50-70°E and 30-40°S when using *F* of -0.01 (Fig. 9a). The zero stresses appear near the crater rim apart from the eastern side and the positive σ_1 extend eastward about 900 km from the crater rim. The orientations of σ_1 are NW-SE direction in the southern and central areas of the crater, NE-SW direction in the northern area and nearly east-west direction in the eastern area.

Except for the compressed Elysium Mons, the extension stresses (positive σ_1) dominate the Utopia basin and its surrounding regions in the northern lowlands (Figs. 9d-f). In most areas of the Utopia basin, the extension stresses are in NE-SW direction, which are almost perpendicular to the dichotomy boundary (Andrews-Hanna et al., 2008). The nearly north-south oriented σ_1 are observed in the eastern region, and NW-SE oriented σ_1 occur in the northern region.

The near-symmetrical distributions of the principal stress directions observed in both the Isidis and Argyre basins (middle and right columns of Figs. 9) suggest the relative simplicity of the modifying processes. However, the mascon-like gravity high (Fig. 1b) and the significantly thinned crust (Figs. 6a-c and 8c) in the Isidis basin implied the dramatic

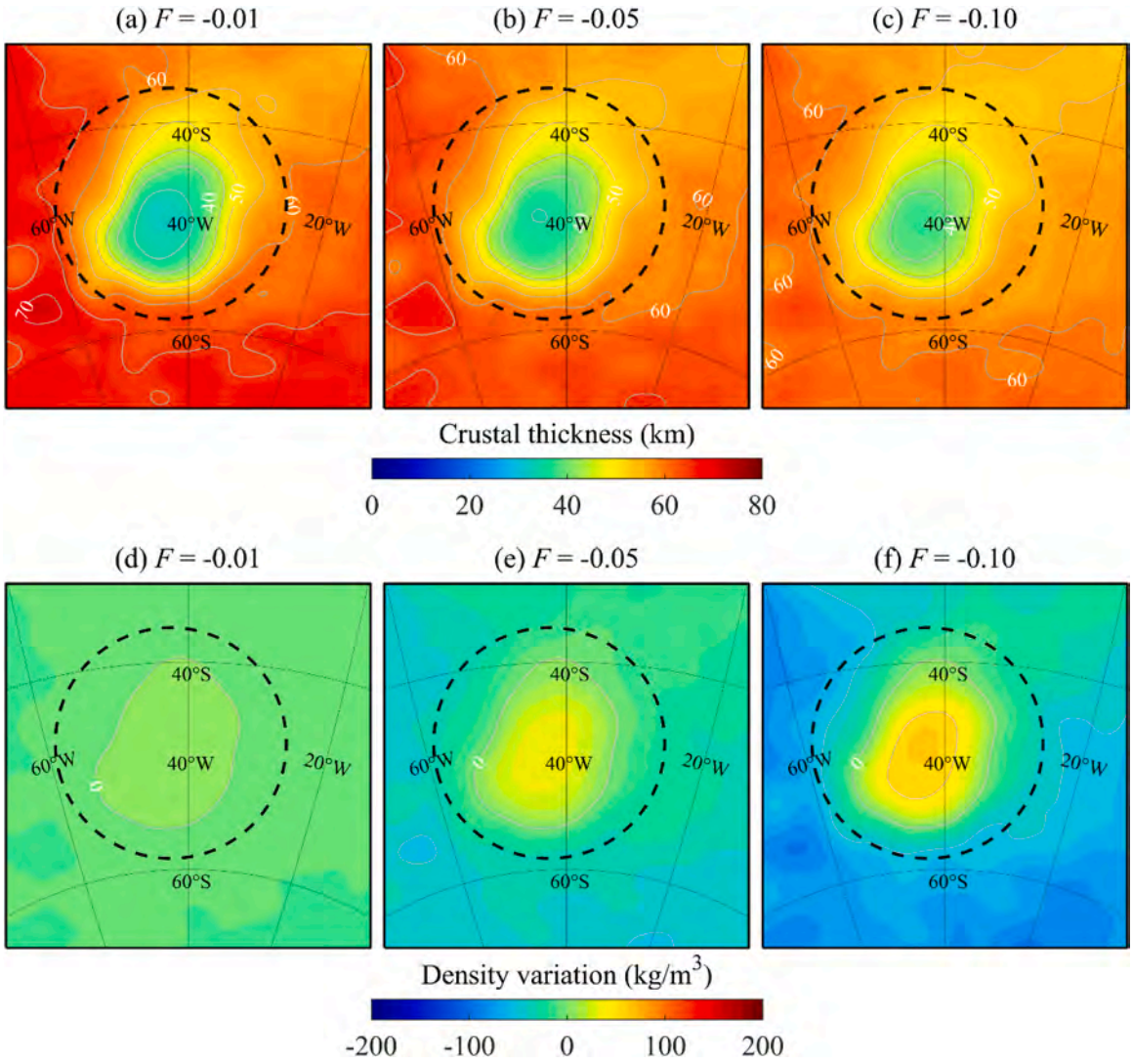

Fig. 7. Same as Fig. 5 but for the Argyre basin.

surface loading and/or isostatic adjustment of the underlying crust. For the Argyre basin, the negative principal stresses presented in the regions of the crater wall (Figs. 9g-i). The similar orientations of σ_1 are found in these two basins. For the Isidis basin, the NW-SE and NE-SW oriented σ_1 are located in the north and south regions, respectively (Figs. 9d-f). On the contrary, the NE-SW and NW-SE oriented σ_1 are located in the north and south regions of the Argyre basin (Figs. 9g-i).

5. Discussion

5.1. Strength of the lithosphere

We firstly compare the observed admittances at the global scale with those theoretical models of Airy, Pratt and flexural isostasy. The admittances suggest that the Mars may be a planet with weak lithosphere with elastic lithosphere thickness of ~10 km without regarding Tharsis Rise (Figs. 4c and 4f). The low strength is consistent with the lithospheric properties of the Tyrrhena Patera (Grott and Wieczorek, 2012), Hellas basin (Searls et al., 2006) and Hesperoa Planum (Broquet and Andrews-Hanna, 2023) in the southern highlands. In addition, McGovern et al. (2002) estimated the elastic lithosphere thickness of 0~10 km for the southern highlands. In the northern lowlands, the elastic lithosphere thickness is near 0 km for the Utopia basin with denser crust estimated by Deng et al. (2023). On the contrary, the elastic lithosphere thickness is at a wide range in serveral previous studies. Turcotte et al. (2002) argued that the elastic lithosphere thickness is equal to the average crustal thickness of ~90 km. Additionally, the estimated elastic lithosphere thickneses are 100-180 km for the Isidis basin (Ritzer and Hauck, 2009) and more than 100 km for several geological units in the northern lowlands (Ding et al., 2019). Although we apply 10 km during the calculations of crustal structures and stresses according to our admittance analysis, the results with different elastic lithosphere thickness are also presented in the Supplementary Material (Figs. S4-S13). The results derived from elastic lithosphere thicknesses of 10, 50 and 100 km present few differences in the crustal thicknesses when using the same *F*, and the short-wavelength signals of density variations and stresses are gradually masked with increasing elastic lithosphere thickness. Therefore, the results with elastic lithosphere thickness of 10 km reveal more detailed characteristics of the crustal structure and stress distribution and may suggest the weak lithosphere of the giant impact basins. The multi-ring structure of the HUIA basins (Frey, 2008) is further evidence, as the formation of which required a weak lithosphere (Melosh and Ivanov, 1999).

5.2. Post-impact crustal accommodation of HUIA basins

Long-wavelength depression in the northern lowlands is produced by an internal mechanism (Smith et al., 1999; Zhong and Roberts, 2003) or

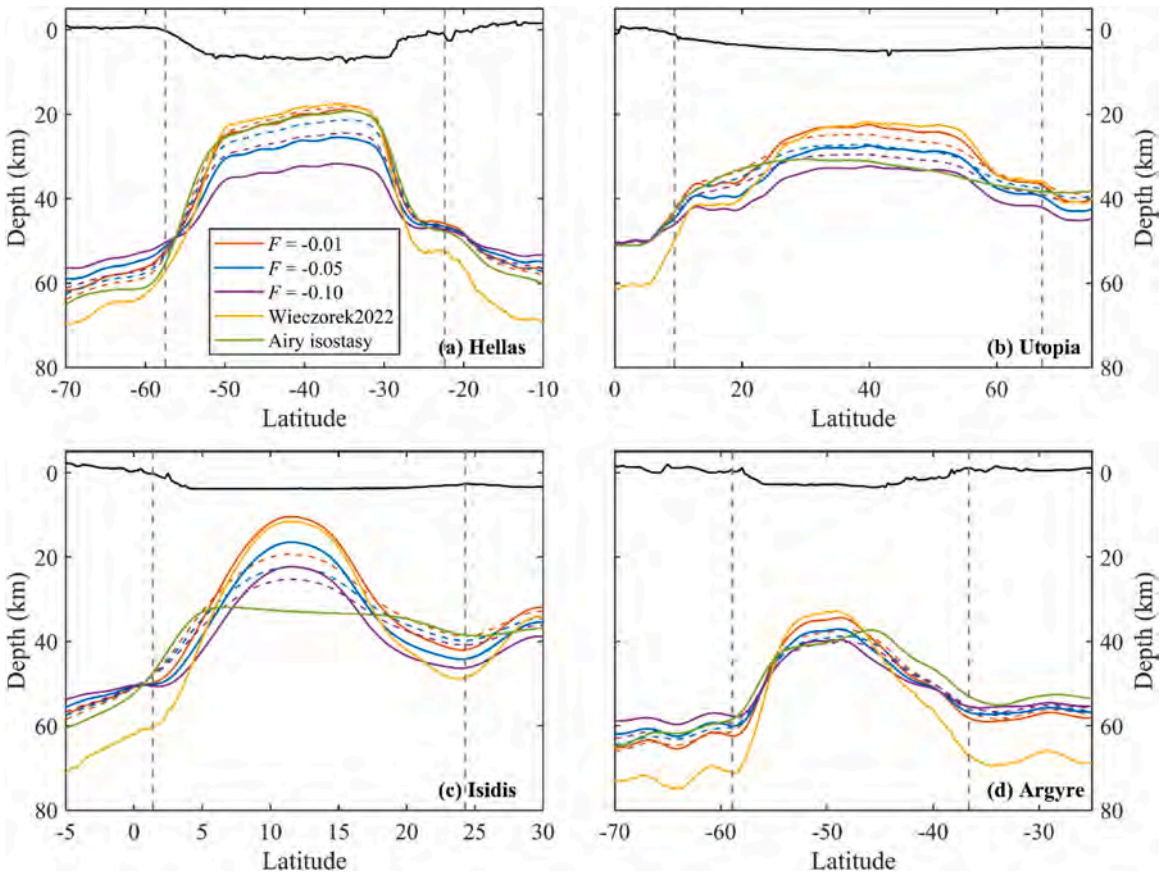

Fig. 8. North-south trending Moho depth profiles across the centers of (a) Hellas, (b) Utopia, (c) Isidis and (d) Argyre basins. The Moho relief is sum of crustal root variation and lithospheric flexure, and the dashed curves with the corresponding color are from the lithospheric flexure only. The Moho depth named Wieczorek2022 is from Mars_thick_Khan2022_39_2900_2900 of Wieczorek et al. (2022) and Airy isostasy is derived from topography shown in Fig. 1a. The doshed grey lines represent the rims of the craters.

a giant impact (Andrews-Hanna et al., 2008). In any case, the HUIA basins formed after establishment of the crustal dichotomy (Andrews-Hanna et al., 2008; Bottke and Andrews-Hanna, 2017; Frey, 2008; Frey et al., 2002; Solomon et al., 2005). Obviously, the "pre--thinned crust" (Frey, 2008) most likely appears beneath the Utopia basin in the northern lowlands. The impactors that produced the Hellas and Argyre basins may have collided with normal Martain crust. It is uncertain whether the northern margin of the Isidis basin exists on the "pre-thinned crust". If the paleoshoreline is taken as the dichotomy boundary (Figs. 1a-c), the HUIA basins can be simply classified into two categories: the first is the Utopia and Isidis basins with mascon-like gravity anomaly in the northern lowlands, the other is the Hellas and Argyre basins with negligible gravity anomaly in the southern highlands (Fig. 1b). However, the multiple characteristics in the crustal thickness of the HUIA basins (e.g. Fig. 8) reveal the diverse mechniums of crustal accommodation, although they are controlled by the extension stresses (Fig. 9).

Giant impact produced melts would be elevated onto the surface when the isostatic adjustment is faster than the magma pond cooling (Tonks and Melosh, 1993). During the timescale of ~10 Myr for post-impact viscoelastic relaxation, the isostatic adjustment due to the deficit mass and the cooling of the impact melts result in the uplift of the entire basin (e.g. Melosh et al., 2013). Even with the backfilling of the excavated materials (Melosh, 1982), the crustal deficit leads to subsequent thinning through the isostatic adjustment. If Airy isostasy is taken as the mechanism of crustal accommodation only, the Moho relief with normal crustal density (e.g. $F = -0.01$) is completely consistent with the isostatic Moho in the Hellas basin (Fig. 8a), suggesting the fully compensation of this basin (Deng et al., 2023; Searls et al., 2006). The diffences in Moho relief from our model and Airy isostasy under the inner Utopia, Isidis and Argyre basins (Figs. 8b-d) indicate that the overcompensated crust should be accommodated by other type mechanisms.

Several previous studies suggest the positive gravity anomaly (Fig. 1b) in the Utopia and Isidis basins are likely the result of volcanic infilling (Ding et al., 2019; Ritzer and Hauck, 2009; Searls et al., 2006). The two basins are considered as the volcanic but not the typical basaltic plains (Grizzaffi and Schultz, 1989). We consider the basin fill to understand the mascon-like gravity anomaly, although the denser lherzolite resulted from difference of the impact magma may exist in the lower crust (Bernadet et al., 2025). The lavas erupted by the Elysum province cover hundreds of meters of the Central Elysium Planitia (Vaucher et al., 2009). A large circum-Isidis volcanic province was completed in Hesperian Period (Ivanov et al., 2012). Another magma source is the magma chamber beneath the Syrtis Major west to Isidis basin (Kiefer, 2004). The large amounts of basaltic magma produced by the widely distributed volcanic activities flowed into the Utopia and Isidis basins. The denser fill would increase the gravity anomaly (Fig. 1b) and crustal density (Fig. 6). We assume the thickness of the basalt filling of ~3 km with 3100 kg/m^3 in the Utopia basin (Ding et al., 2019; Searls et al., 2006) and the elavation of -6 km for the basin floor. Subsequently, the crustal root variations would be about 14.9, -1.7 and -4.4 km for F of -0.01, -0.05 and -0.1, respectively. The results of the last two are consistent with those of our model (Fig. 8b). At F of -0.05, the equivalent filling density with thickness of 3 km is ~3200 kg/m^3 comparable to that of shergottites when using the crustal thickness of ~30 km (Fig. 6b) and density variation of larger than 100 kg/m^3 (Fig. 6e), agreeing with the basalt density. However, the equivalent filling density is unreasonable

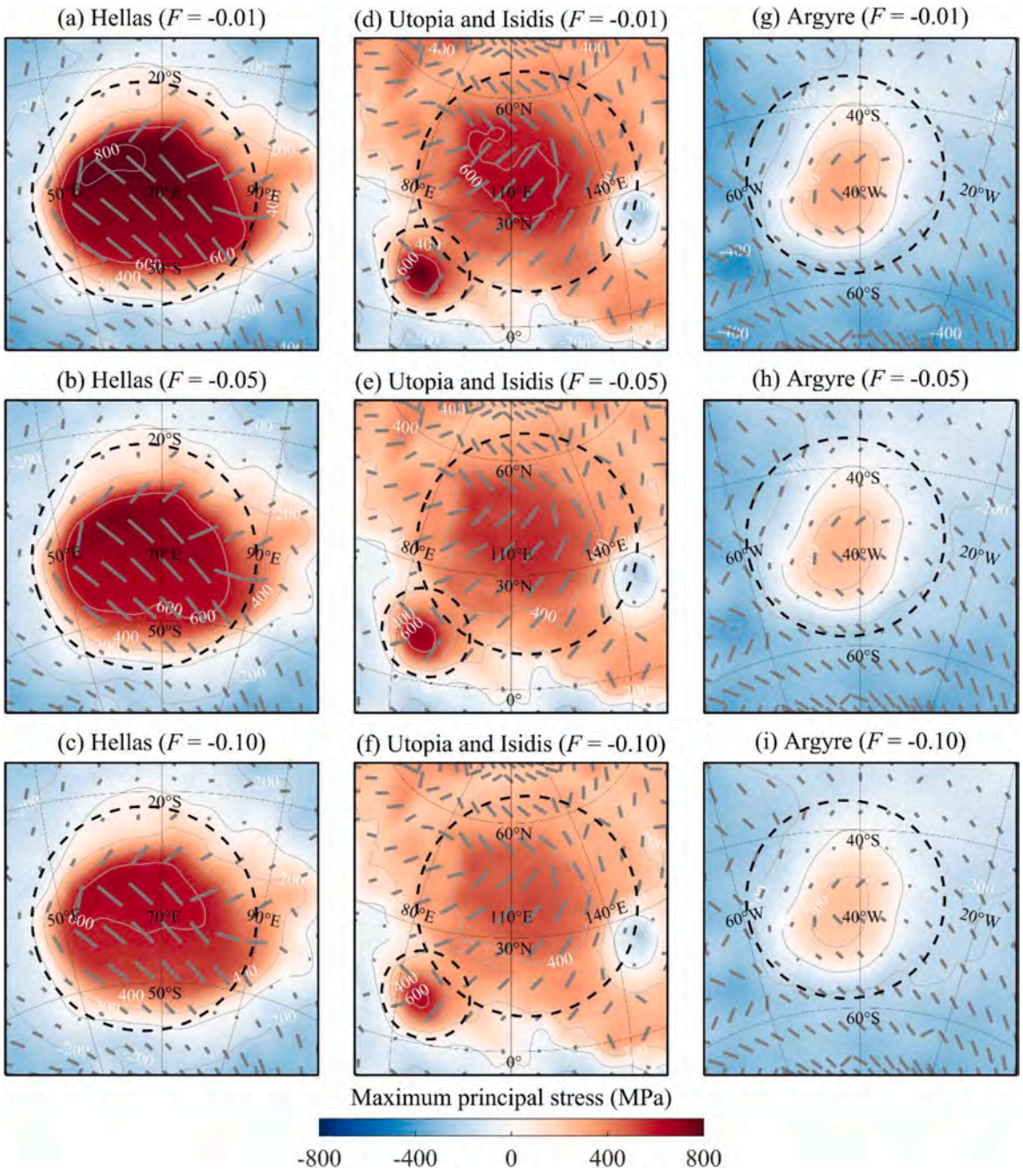

Fig. 9. Maximum principal stress of the HUIA basins. The short gray lines indicate the direction of the principal stress.

when using the crustal thickness of ~30 km (Fig. 6c) and density variation of larger than 100 kg/m^3 (Fig. 6f). Therefore, we suggest that the basalt magma fill is an important factor in the crustal modification of the Utopia basin. Similarly, the Isidis basin may have the denser basalt filling (Potts et al., 2004) and the filled elevation higher than that in the Utopia basin due to the possibly topography-inferred flow channel (Fig. 1a). The approximately axisymmetrical stresses with larger values of the Isidis basin (Figs. 9d-f) suggest the crustal deformation is basically dominated by the radial mechanisms.

It is note that little remained Moho relief appear under most large impact basins with 275-1000 km in diameter (McGovern et al., 2002; Mohit and Phillips, 2007). Mohit and Phillips (2007) suggested that the modified Moho relief results from the viscous relaxation of the lower crust. Significant lateral heterogeneity in crustal structures of the HUIA basins (Figs. 5-7) indicate the absence or few amount of the relaxed lower crust. Low surface heat flow would not satisfy the viscous relaxation of the lower crust due to the sufficient temperature. Particularly, the crustal relaxation would occur beneath the Argyre basin in the case of the higher heat production rate (Grott and Breuer, 2008a), where the crust is relative thick (e.g., Fig. 8) and the surface heat flow is larger than other three basins (Plesa et al., 2018). Using surface heat flow of 25 mW m^{-2} (Plesa et al., 2018), heat production rate of 58 pW kg^{-1} (Grott and Breuer, 2008a) and crustal thermal conductivity of 2.5 W m^{-1} K^{-1} (McGovern et al., 2002), the temperature would be ~600 K at the location of maximum Moho uplift of the Argyre basin. The viscous relaxation would likely occur for the wet diabase lower crust (Grott and Breuer, 2008b), agreeing with slight Moho uplift relative to the isostatic Moho (Fig. 8d) due to the high temperature. Therefore, we suggest the crustal structures in the Argyre basin should be low subsurface loads (Fig. 7a and 7d) accommodated by the isostatic compensation and

viscous relaxation of the lower crust. The approximately north-south symmetrical stresses of the Argyre basin and the compression stresses presented in wall region (Figs. 9g-i) suggest the relaxed crust may a secondary role in the post-impact crustal deformation.

6. Conclusions

In this study, we present the observed admittances and the theoretical Airy, Pratt and flexural admittances at global scale. By removing the effects of Tharsis Rise, we deduce a low elastic lithosphere thickness for both the northern lowlands and southern highlands from the low- and intermediate-degree results. Applying an elastic lithosphere thickness of 10 km, we obtain the crustal structures and lithospheric stresses based on the thin-shell model proposed by Banerdt (1986). The results show the significant Moho relief, extensional and hydrostatic lithosphere in the HUIA basins, and provide insights into how giant impacts reshaped the Martian crust and how subsequent processes modified these structures. By comparing with the isostatic crustal structures, isostatic adjustment, viscous relaxation of the lower crust and basalt fill are the post-impact accommodations of the crust, among which isostatic adjustment is the dominate mechanism for the Moho uplift. In the southern highlands, Hellas demonstrates Airy-type isostatic compensation, contrasting with Argyre's crust which shows evidence of viscoelastic relaxation. Denser volcanic infilling of the Utopia and Isidis basins may be the major contribution to the positive gravity anomaly.

CRediT authorship contribution statement

Songbai Xuan: Writing – original draft, Software, Methodology, Investigation, Funding acquisition. **Shuanggen Jin:** Writing – review & editing, Supervision, Funding acquisition, Conceptualization.

Declaration of competing interest

None.

Acknowledgements

We would like to thank two anonymous reviewers for their comments and suggestions, which helped to improve the manuscript. S.X. would like to thank Prof. Jin Li for invaluable discussions. This work is supported by the National Key Research and Development Program of China (Grant No. 2021YFA0716100), National Natural Science Foundation of China (Grant No. 42074090) and Open Fund of Wuhan, Gravitation and Solid Earth Tides, National Observation and Research Station (Grant No. WHYWZ202207).

Supplementary materials

Supplementary material associated with this article can be found, in the online version, at doi:10.1016/j.epsl.2025.119567.

Data availability

Data will be made available on request.

References

Andrews-Hanna, J.C., Zuber, M.T., Banerdt, W.B., 2008. The Borealis basin and the origin of the martian crustal dichotomy. Nature 453, 1212–1215.
Arkani-Hamed, J., 2000. Strength of Martian lithosphere beneath large volcanoes. J. Geophys. Res. Planets 105, 26713–26732.
Audet, P., 2014. Toward mapping the effective elastic thickness of planetary lithospheres from a spherical wavelet analysis of gravity and topography. Phys. Earth Planet. Inter. 226, 48–82.
Banerdt, W.B., 1986. Support of long-wavelength loads on Venus and implications for internal structure. J. Geophys. Res. 91, 403–419.
Belleguic, V., Lognonne, P., Wieczorek, M., 2005. Constraints on the Martian lithosphere from gravity and topography data. J. Geophys. Res. Planets 110, E11005.
Bernadet, J., Borisova, A.Y., Guitreau, M., Safonov, O.G., Asimow, P., Nedelec, A., Bohrson, W.A., Kosova, S.A., de Parseval, P., 2025. Making continental crust on water-bearing terrestrial planets. Sci. Adv. 11, eads6746.
Bottke, W.F., Andrews-Hanna, J.C., 2017. A post-accretionary lull in large impacts on early Mars. Nat. Geosci. 10, 344–348.
Bottke, W.F., Norman, M.D., 2017. The late heavy bombardment. Annu. Rev. Earth Planet. Sci. 45, 619–647.
Broquet, A., Andrews-Hanna, J.C., 2022. Geophysical evidence for an active mantle plume underneath Elysium Planitia on Mars. Nat. Astron. 160–169.
Broquet, A., Andrews-Hanna, J.C., 2023. Plume-induced flood basalts on hesperian Mars: an investigation of Hesperia Planum. Icarus 391, 115338.
Broquet, A., Wieczorek, M.A., 2019. The gravitational signature of martian volcanoes. J. Geophys. Res. Planets 124, 2054–2086.
Crane, K., Rich, J., 2023. Lithospheric strength and elastic properties for Mars from InSight geophysical data. Icarus 400, 115581.
Deng, Q.Y., Zhong, Z., Ye, M., Zhang, W.S., Qiu, D.G., Zheng, C., Yan, J.G., Li, F., Barriot, J.P., 2023. Lithospheric loading model for large impact basins where a mantle plug is present. J. Geophys. Res. Planets 128 e2022JE007620.
Ding, M., Lin, J., Gu, C., Huang, Q.H., Zuber, M.T., 2019. Variations in martian lithospheric strength based on gravity/topography analysis. J. Geophys. Res. Planets 124, 3095–3118.
Forsyth, D.W., 1985. Subsurface loading and estimates of the flexural rigidity of continental lithosphere. J. Geophys. Res. 90, 12623–12632.
Frey, H., 2008. Ages of very large impact basins on Mars: implications for the late heavy bombardment in the inner solar system. Geophys. Res. Lett. 35, L13203.
Frey, H.V., Roark, J.H., Shockey, K.M., Frey, E.L., Sakimoto, S.E.H., 2002. Ancient lowlands on Mars. Geophys. Res. Lett. 29, 1384.
Goossens, S., Sabaka, T.J., Genova, A., Mazarico, E., Nicolas, J.B., Neumann, G.A., 2017. Evidence for a low bulk crustal density for Mars from gravity and topography. Geophys. Res. Lett. 44, 7686–7694.
Grizzaffi, P., Schultz, P.H., 1989. Isidis Basin: site of ancient volatile-rich debris layer. Icarus 77, 358–381.
Grott, M., Breuer, D., 2008a. Constraints on the radiogenic heat production rate in the Martian interior from viscous relaxation of crustal thickness variations. Geophys. Res. Lett. 35. L05201.
Grott, M., Breuer, D., 2008b. The evolution of the martian elastic lithosphere and implications for crustal and mantle rheology. Icarus 193, 503–515.
Grott, M., Wieczorek, M.A., 2012. Density and lithospheric structure at Tyrrhena Patera, Mars, from gravity and topography data. Icarus 221, 43–52.
Harig, C., Lewis, K.W., Plattner, A., Simons, F.J., 2015. A suite of software analyzes data on the sphere. Eos (Wash. DC) 96, 18–22.
Hemingway, D.J., Matsuyama, I., 2017. Isostatic equilibrium in spherical coordinates and implications for crustal thickness on the Moon, Mars, Enceladus, and elsewhere. Geophys. Res. Lett. 44, 7695–7705.
Hoogenboom, T., Srnrekar, S.E., 2006. Elastic thickness estimates for the northern lowlands of Mars. Earth Planet. Sci. Lett. 248, 830–839.
Ivanov, M.A., Hiesinger, H., Erkeling, G., Hielscher, F.J., Reiss, D., 2012. Major episodes of geologic history of Isidis Planitia on Mars. Icarus 218, 24–46.
Jin, S.G., Zhang, T.Y., 2014. Automatic detection of impact craters on Mars using a modified adaboosting method. Planet. Space Sci. 99, 112–117.
Kiefer, W.S., 2004. Gravity evidence for an extinct magma chamber beneath Syrtis Major, Mars: a look at the magmatic plumbing system. Earth Planet. Sci. Lett. 222, 349–361.
Knapmeyer-Endrun, B., Panning, M.P., Bissig, F., Joshi, R., Khan, A., Kim, D., Lekic, V., Tauzin, B., Tharimena, S., Plasman, M., Compaire, N., Garcia, R.F., Margerin, L., Schimmel, M., Stutzmann, E., Schmerr, N., Bozdag, E., Plesa, A.C., Wieczorek, M.A., Broquet, A., Antonangeli, D., McLennan, S.M., Samuel, H., Michaut, C., Pan, L., Smrekar, S.E., Johnson, C.L., Brinkman, N., Mittelholz, A., Rivoldini, A., Davis, P.M., Lognonne, P., Pinot, B., Scholz, J.R., Stahler, S., Knapmeyer, M., van Driel, M., Giardini, D., Banerdt, W.B., 2021. Thickness and structure of the martian crust from InSight seismic data. Science 373, 438–443.
Konopliv, A.S., Park, R.S., Folkner, W.M., 2016. An improved JPL Mars gravity field and orientation from Mars orbiter and lander tracking data. Icarus 274, 253–260.
Mancinelli, P., Mondini, A.C., Pauselli, C., Federico, C., 2015. Impact and admittance modeling of the Isidis Planitia, Mars. Planet. Space Sci. 117, 73–81.
McGovern, P.J., Solomon, S.C., Smith, D.E., Zuber, M.T., Simons, M., Wieczorek, M.A., Phillips, R.J., Neumann, G.A., Aharonson, O., Head, J.W., 2002. Localized gravity/topography admittance and correlation spectra on Mars: implications for regional and global evolution. J. Geophys. Res. Planets 107, 5136.
McKenzie, D., Barnett, D.N., Yuan, D.N., 2002. The relationship between Martian gravity and topography. Earth Planet. Sci. Lett. 195, 1–16.
Melosh, H.J., 1982. A schematic model of crater modification by gravity. J. Geophys. Res. 87, 371–380.
Melosh, H.J., Freed, A.M., Johnson, B.C., Blair, D.M., Andrews-Hanna, J.C., Neumann, G. A., Phillips, R.J., Smith, D.E., Solomon, S.C., Wieczorek, M.A., Zuber, M.T., 2013. The origin of Lunar mascon basins. Science 340, 1552–1555.
Melosh, H.J., Ivanov, B.A., 1999. Impact crater collapse. Annu. Rev. Earth Planet. Sci. 27, 385–415.
Mohit, P.S., Phillips, R.J., 2007. Viscous relaxation on early Mars: a study of ancient impact basins. Geophys. Res. Lett. 34, L21204.
Neumann, G.A., Zuber, M.T., Wieczorek, M.A., McGovern, P.J., Lemoine, F.G., Smith, D. E., 2004. Crustal structure of Mars from gravity and topography. J. Geophys. Res. Planets 109, E8002.

Parker, T.J., Gorsline, D.S., Saunders, R.S., Pieri, D.C., Schneeberger, D.M., 1993. Coastal geomorphology of the Martian Northern Plains. J. Geophys. Res. Planets 98, 11061–11078.
Pauer, M., Fleming, K., Cadek, O., 2006. Modeling the dynamic component of the geoid and topography of Venus. J. Geophys. Res. Planets 111, E11012.
Phillips, R.J., Zuber, M.T., Solomon, S.C., Golombek, M.P., Jakosky, B.M., Banerdt, W.B., Smith, D.E., Williams, R.M.E., Hynek, B.M., Aharonson, O., Hauck, S.A., 2001. Ancient geodynamics and global-scale hydrology on Mars. Science 291, 2587–2591.
Plesa, A.C., Padovan, S., Tosi, N., Breuer, D., Grott, M., Wieczorek, M.A., Spohn, T., Smrekar, S.E., Banerdt, W.B., 2018. The thermal state and interior structure of Mars. Geophys. Res. Lett. 45, 12198–12209.
Potts, L.V., von Frese, R.R., Leftwich, T.E., Taylor, P.T., Shum, C.K., Li, R.X., 2004. Gravity-inferred crustal attributes of visible and buried impact basins on Mars. J. Geophys. Res. Planets 109. E09009.
Ritzer, J.A., Hauck, S.A., 2009. Lithospheric structure and tectonics at Isidis Planitia, Mars. Icarus 201, 528–539.
Searls, M.L., Banerdt, W.B., Phillips, R.J., 2006. Utopia and Hellas basins, Mars: twins separated at birth. J. Geophys. Res. Planets 111. E08005.
Sholes, S.F., Dickeson, Z.I., Montgomery, D.R., Catling, D.C., 2021. Where are Mars' Hypothesized ocean shorelines? Large lateral and topographic offsets between different versions of paleoshoreline maps. J. Geophys. Res. Planets 126 e2020JE006486.
Simons, F.J., Dahlen, F.A., Wieczorek, M.A., 2006. Spatiospectral concentration on a sphere. SIAM Rev. 48, 504–536.
Sleep, N.H., Phillips, R.J., 1985. Gravity and lithospheric stress on the terrestrial planets with reference to the Tharsis region of Mars. J. Geophys. Res. 90, 4469–4489.
Smith, D.E., Zuber, M.T., Solomon, S.C., Phillips, R.J., Head, J.W., Garvin, J.B., Banerdt, W.B., Muhleman, D.O., Pettengill, G.H., Neumann, G.A., Lemoine, F.G., Abshire, J.B., Aharonson, O., Brown, C.D., Hauck, S.A., Ivanov, A.B., McGovern, P.J., Zwally, H.J., Duxbury, T.C., 1999. The global topography of Mars and implications for surface evolution. Science 284, 1495–1503.
Solomon, S.C., Aharonson, O., Aurnou, J.M., Banerdt, W.B., Carr, M.H., Dombard, A.J., Frey, H.V., Golombek, M.P., Hauck, S.A., Head, J.W., Jakosky, B.M., Johnson, C.L., McGovern, P.J., Neumann, G.A., Phillips, R.J., Smith, D.E., Zuber, M.T., 2005. New perspectives on ancient Mars. Science 307, 1214–1220.
Tanaka, K.L., Robbins, S.J., Fortezzo, C.M., Skinner, J.A., Hare, T.M., 2014. The digital global geologic map of Mars: chronostratigraphic ages, topographic and crater morphologic characteristics, and updated resurfacing history. Planet. Space Sci. 95, 11–24.
Tenzer, R., Eshagh, M., Jin, S.G., 2015. Martian sub-crustal stress from gravity and topographic models. Earth Planet. Sci. Lett. 425, 84–92.
Tonks, W.B., Melosh, H.J., 1993. Magma Ocean formation due to giant impacts. J. Geophys. Res. Planets 98, 5319–5333.
Turcotte, D.L., Shcherbakov, R., Malamud, B.D., Kucinskas, A.B., 2002. Is the Martian crust also the Martian elastic lithosphere? J. Geophys. Res. Planets 107, 5091.
Turcotte, D.L., Willemann, R.J., Haxby, W.F., Norberry, J., 1981. Role of membrane stresses in the support of planetary topography. J. Geophys. Res. 86, 3951–3959.
Vaucher, J., Baratoux, D., Mangold, N., Pinet, P., Kurita, K., Gregoire, M., 2009. The volcanic history of central Elysium Planitia: implications for martian magmatism. Icarus 204, 418–442.
Werner, S.C., 2008. The early martian evolution—constraints from basin formation ages. Icarus 195, 45–60.
Werner, S.C., 2009. The global martian volcanic evolutionary history. Icarus 201, 44–68.
Wieczorek, M.A., 2015. Gravity and topography of the terrestrial planets. Ed.. In: Schubert, G. (Ed.), Treatise on Geophysics. Elsevier, pp. 153–193 (Second Edition).
Wieczorek, M.A., Broquet, A., McLennan, S.M., Rivoldini, A., Golombek, M., Antonangeli, D., Beghein, C., Giardini, D., Gudkova, T., Gyalay, S., Johnson, C.L., Joshi, R., Kim, D., King, S.D., Knapmeyer-Endrun, B., Lognonne, P., Michaut, C., Mittelholz, A., Nimmo, F., Ojha, L., Panning, M.P., Plesa, A.C., Siegler, M.A., Smrekar, S.E., Spohn, T., Banerdt, W.B., 2022. InSight constraints on the global character of the martian crust. J. Geophys. Res. Planets 127 e2022JE007298.
Wieczorek, M.A., Simons, F.J., 2005. Localized spectral analysis on the sphere. Geophys. J. Int. 162, 655–675.
Zhong, S.J., Roberts, J.H., 2003. On the support of the Tharsis Rise on Mars. Earth Planet. Sci. Lett. 214, 1–9.
Zhong, Z., Yan, J.G., Liu, X.F., Chen, S.G., Fan, G.X., Yang, C., Pang, L.J., Barriot, J.P., 2022. The ancient martian lithospheric structure at Isidis Planitia. Icarus 374, 114741.
Zuber, M.T., Smith, D.E., 1997. Mars without Tharsis. J. Geophys. Res. Planets 102, 28673–28685.
Zuber, M.T., Solomon, S.C., Phillips, R.J., Smith, D.E., Tyler, G.L., Aharonson, O., Balmino, G., Banerdt, W.B., Head, J.W., Johnson, C.L., Lemoine, F.G., McGovern, P. J., Neumann, G.A., Rowlands, D.D., Zhong, S.J., 2000. Internal structure and early thermal evolution of Mars from Mars Global Surveyor topography and gravity. Science 287, 1788–1793.